Environmental Science Processes & Impacts

ROYAL SOCIETY OF CHEMISTRY

PAPER

View Article Online
View Journal | View Issue

Check for updates

Cite this: *Environ. Sci.: Processes Impacts*, 2021, **23**, 1488

Particle characterisation and bioaccessibility of manganese in particulate matter in silico- and ferromanganese smelters†

Stine Eriksen Hammer, [a] Torunn Ervik, *[a] Dag G. Ellingsen,[a] Yngvar Thomassen,[a] Stephan Weinbruch,[ab] Nathalie Benker[b] and Balazs Berlinger ‡[a]

The aim of this study was to characterise particulate matter (PM) collected in the furnace area during SiMn and high carbon (HC)–FeMn production in terms of single particle analysis and to determine the bioaccessibility of Mn in the PM in a simulated lung fluid. Airborne PM was collected with Sioutas cascade impactors and respirable cyclones in the breathing zone of tappers and crane operators. Stationary samples were collected from the furnace area with a nanoMOUDI cascade impactor and an ESPnano electrostatic particle collector. Individual particles were characterised by scanning and transmission electron microscopy. Bioaccessibility of Mn was studied in terms of the dissolution of Mn in Gamble solution (24 hours leaching at 37 °C) relative to total Mn. Slag particles, alloy fragments, Mn and Fe oxides as well as carbonaceous particles were observed in the size fraction > 1 μm aerodynamic diameter (d_{ae}). Thermally generated condensation particles dominated the d_{ae} size range of 0.18–1 μm collected from the tapping fumes, while carbonaceous particles dominated the fraction below 0.18 μm. Condensation generated particles from the furnace area of HC–FeMn production were coated with an amorphous Si–O rich surface layer which seemed to hold primary particles together as aggregates. In the same size range, the particles from the furnace area of SiMn production were dominated by spherical condensation particles rich in Si, Mn and O, but without a Si–O rich surface layer. Instead, the Mn oxides were enclosed in an amorphous Si–O rich matrix. The bioaccessibility of Mn was low to moderate (<30%), but higher for SiMn furnace workers (highest median = 23%) than HC–FeMn furnace workers (highest median = 12%). This difference in bioaccessibility was significant for PM with d_{ae} up to 2.5 μm, and most pronounced in the d_{ae} size range between 0.25 and 1.0 μm. Also, a significantly higher bioaccessibility of Mn was found for PM larger than d_{ae} of 0.5 μm collected among crane operators compared to tappers in the HC–FeMn smelter.

Received 21st June 2021
Accepted 1st September 2021

DOI: 10.1039/d1em00243k

rsc.li/espi

Environmental significance

Adverse health effects on the central nervous system caused by manganese exposure depend on the exposure dose, chemical composition and bioavailability of manganese. To investigate this in an occupational setting, the bioaccessibility of manganese in particulate matter has been investigated in terms of dissolution in Gamble's solution. The particulate matter was collected and size fractionated in the breathing zone of workers in manganese smelters. Particle size is important for deposition in the respiratory tract. In addition, individual particles collected using stationary equipment were characterised. Knowledge of physical and chemical properties of particles combined with information on the bioaccessibility is fundamental to understanding exposure–response associations.

1 Introduction

Studies on rats have shown that exposure to soluble manganese (Mn) results in higher Mn concentration in the brain than exposure to less soluble Mn.[1,2] In humans, exposure to Mn is of health concern. Adverse health effects on the central nervous system associated with Mn exposure have been reported in *e.g.* welders,[3–6] miners,[7,8] battery industry workers[9,10] as well as workers in the Mn alloy producing industry.[11–13] These adverse

[a]*National Institute of Occupational Health, Gydas vei 8, N-0363 Oslo, Norway. E-mail: torunn.ervik@stami.no*

[b]*Institute of Applied Geosciences, Technical University of Darmstadt, Schnittspahnstrasse 9, D-64287 Darmstadt, Germany*

† Electronic supplementary information (ESI) available. See DOI: 10.1039/d1em00243k

‡ Current address: Soos Research and Development Center, University of Pannonia, Zrinyi Miklos str. 18, H-8800 Nagykanizsa, Hungary.

health effects depend on the exposure dose, chemical composition and bioavailability of Mn.

Ferro- and silicomanganese (FeMn and SiMn) are essential additives in steelmaking used to provide specific properties of steel.[14] High carbon (HC)–FeMn and SiMn are mainly produced in electric submerged arc furnaces with coke to facilitate the reduction of Mn oxide ores. Other raw materials include fluxes such as dolomite, calcite and quartz in SiMn production and lime in FeMn production. In addition, Mn-rich slag from FeMn production is recycled as feedstock in SiMn production.[15] Thermally generated fumes are emitted during tapping, refining and casting of the alloys.[16]

Previous studies on HC–FeMn and SiMn production showed that the abundance of different particle types strongly depends on the size fraction. HC–FeMn tapping fume particles larger than 0.3 μm were dominated by slag particles, and generally particles were composed of different mineral phases.[17] A large number of spherical potassium (K)-rich particles with sizes < 1–2 μm as well as irregular fragments of Mn oxides or mixed oxides > 1 μm were observed in HC–FeMn tapping fume.[18] The submicron fraction is dominated by agglomerated Mn oxides, mainly MnO. Similar fume particles were reported by Kero *et al.* (2015),[20] where MnO, MnO_x-FeO_y, and Mn_3O_4 were identified depending on the temperature and location during formation, *e.g.* crucible and filter. According to Ervik *et al.*[19] the predominant phase in the submicron fraction was Mn_3O_4. In SiMn production, fume from the casting process is composed of slag particles and slag mixed with C-rich particles dominating the size fraction above 0.3 μm.[17,18] The submicron fraction was found to be dominated by agglomerated Mn–Si phases.[18] Kero *et al.*[20] investigated the size distribution and found that agglomerated spheres dominate the aerodynamic diameter (d_{ae}) size range from 0.09 to 0.94 μm. The majority of the SiMn fume particles consisted of Mn, Si and O. Furthermore, SiMn fume thermally generated in a laboratory scale experiment was studied by Ma *et al.*[21] The particle types generated depended on the melt temperature and on the collection position inside their experimental furnace setup. Also, a mixture of Mn– and Mn–Si oxides in both crystalline and amorphous states was observed by X-ray diffraction.

Bioaccessibility is the fraction of a compound released from its matrix becoming available for absorption in the body.[22] Bioaccessibility of Mn in the respirable aerosol fraction is of interest since it is a measure of the amount of Mn available for absorption into the systemic circulation *via* the lungs. In laboratory studies, the bioaccessibility depends on the choice of simulated lung fluid.[23] In such studies, different simulated lung fluids have been used, with Gamble solution (pH 7.4) being the most used simulated interstitial lung fluid.[24] Gamble solution[25] consists of an electrolyte composition simulating the human interstitial fluid,[26] but lacks phospholipids which are the most abundant components of the alveolar lining fluid.[27]

The bioaccessibility of Mn in airborne PM from HC–FeMn or SiMn production has to our knowledge been sparsely investigated. In a study of ambient air in a heavily industrialised area, the bioaccessibility of metals in PM collected near an FeMn smelter and steel making plant was moderate (20–40%) for Mn.[28] Bioaccessibility of Mn at work places was studied for welding fume[29–31] and in PM from other hot processes.[32] It was shown that the bioaccessibility of Mn was generally low (<20%) to moderate, depending on the origin of exposure and the simulated lung fluid used. Even when the bioaccessible fraction of Mn was low in welding fume, a correlation with the Mn concentration in the urine of the welders was found.[30]

Particle mass size distributions of workplace aerosols in Mn alloy smelters were investigated by Berlinger *et al.*[33] using personal respirable cyclones and a 5-stage cascade impactor. As a follow up study, the chemical composition and bioaccessibility of Mn in terms of dissolution in Gamble solution are investigated in the present paper. Special emphasis is placed on the apparent dissolution of Mn as a function of the production process, particle size distribution and work task. Particles collected at different workplaces in the two smelters were studied in detail by scanning and transmission electron microscopy (SEM and TEM) to better understand the dissolution of Mn in size fractionated PM using Gamble solution.

2 Materials and methods

2.1 Production and work tasks

Air samples were collected in two different Mn alloy producing smelters in Norway, each operating two furnaces. Smelter 1 produces SiMn and HC–FeMn, whereas Smelter 2 produces only HC–FeMn. Every two to three hours molten alloy and slag are tapped from the furnaces and poured into large ladles. The ladles with molten alloy are transported with cranes to the casting area, similar to what is described in Olsen *et al.*[15] Tapping and casting are open processes which emit thermally generated fumes into the furnace hall. The furnace workers included in this study were tappers and crane operators. Depending on the tapping time, tappers and crane operators worked 45–75 minutes on the tapping floor, three to four times during an eight-hour shift, but the crane operators' tasks were conducted further away from the taphole. The crane operators included in this study operated the cranes near the furnace with remote controllers fixed to their shoulders with straps. They were not expected to have significantly different exposure qualitatively than tappers, however, the level of their exposure proved to be significantly different than in the case of tappers. Details on the work tasks have been published by Berlinger *et al.*[33]

2.2 Sampling

In a first sampling campaign, 6–7 hour air samples were collected by personal sampling in the breathing-zone of 19 tappers and 18 crane operators with five-stage Sioutas cascade impactors (SKC, Eighty Four, PA, USA) loaded with 0.5 μm pore size 25 mm polytetrafluoroethylene (PTFE) substrates and a 2.0 μm pore size PTFE filter as an end filter, as well as respirable cyclones (JS Holdings, Stevenage, UK) loaded with 5.0 μm pore size PVC membrane filters (Millipore Corp., Billerica, MA, USA). Leland Legacy model high flow (SJC, Eighty Four, PA, USA) ensured an air sampling flow of 9 L min^{-1} for the Sioutas cascade impactors, and in house-built PS103 sampling pumps (National Institute of Occupational Health, Oslo, Norway) were

operating at the flow rate of 2.2 L min^{-1} for the respirable samples. Details have been published by Berlinger *et al.*[33] Additionally, for Smelter 1, particles were collected on copper (Cu) TEM grids with holey carbon film with a hand-held ESPnano model 100 electrostatic deposition sampler (ESPnano Inc., Spokane, WA, USA) (Miller *et al.*, 2010)[34] with sampling times between 10 and 200 seconds.

In a second sampling campaign conducted only in Smelter 1, stationary air samples were collected for 10 minutes with a 13-stage nanoMOUDI cascade impactor (MSP Corporation, Shoreview, Minnesota, USA) during tapping of both HC–FeMn and SiMn furnaces. The samples were collected around eight meters from the tapping hole. The 50% d_{ae} cut-off for each stage was: 10, 5.6, 3.2, 1.8, 1.0, 0.56, 0.32, 0.18, 0.1, 0.056, 0.032, 0.018 and 0.010 μm. Particles with d_{ae} < 0.010 μm are collected by filtration on an end-filter. Cu TEM grids with holey carbon films (EMresolution, Sheffield, UK) were affixed to the surface of polyvinyl chloride membrane filters used as substrates in all impactor stages, except for the end-filter. TEM grids were not attached to the end-filter because the predominant mass on this stage is bounce off particles from the previous impaction stages.[34] In addition, a TSI Scanning Mobility Particle Sizer (SMPS) instrument (model 3034, TSI Inc., Shoreview, MN, USA) with flow rate 1 L min^{-1} was running for six hours for each furnace in Smelter 1 during the second sampling campaign. The SMPS was placed next to nanoMOUDI, around eight metres from the tapping hole.

2.3 Transmission and scanning electron microscopy

Particles collected with the electrostatic sampler were characterised by SEM and TEM without coating. Individual particles were investigated with a Hitachi SU6600 field emission SEM (Hitachi, Tokyo, Japan) equipped with a Bruker energy-dispersive X-ray (EDX) detector (Bruker Nano GmbH, Berlin, Germany) and an electron backscatter diffraction (EBSD) detector (NORDIF, Trondheim, Norway). A minimum of 200 particles was investigated on each Cu TEM grid collected with the electrostatic sampler. For the cascade impactor samples, a minimum of 200 particles was investigated in the d_{ae} size range 10–1.8 μm (stage 1–4), 1.0–0.18 μm (stage 5–8) and 0.1–0.01 μm (stage 9–13). The phase composition of selected particles was determined by EBSD as described by Ervik *et al.*[36] The samples were also investigated by TEM using a Jeol 2100 F (Tokyo, Japan) instrument (field emission gun) equipped with an EDX silicon drift detector X-Max (Oxford Instruments, Abingdon, UK). The microscope was operated in scanning-TEM (STEM) mode and in TEM modes. The acceleration voltage was 200 kV leading to a point resolution of approximately 0.22 nm. Images were recorded with a charge-coupled device (CCD) camera and treated with Digital Micrograph software (Gatan Inc., Pleasanton, United States) and FIJI image processing software.[37]

2.4 Leaching and digestion procedures of air filters and impactor substrates

Gamble solution was prepared as described by Berlinger *et al.*[29] All samples and blanks were added to 10 mL of Gamble solutusted with 0.1 M HCl and 0.1 M NaOH) in 15 mL polypropylene tubes (Sarstedt, Nümbrecht, Germany) and shaken, before leaving for 24 hours in a laboratory oven set to 37 ± 1 °C. The samples were then filtered through 0.45 μm pore size 25 mm mixed cellulose ester membrane filters (Merck Millipore, Billerica, MA, USA) fixed in Disposable Funnel units (Eichrom Technologies, Lisle, USA) sealed with Teflon tape. One mL nitric acid (puriss p.a., Sigma Aldrich – Merck, Darmstadt, Germany) and 100 μL internal standard solution (germanium 25 mg L^{-1}) were added to the filtrate before dilution to 25 mL with deionised water (18.2 MΩ cm, Merck Millipore, Billerica, MA, USA). The membrane filters with the non-dissolved PM were microwave digested (Multiwave PRO, Anton Paar, Graz, Austria) in temperature controlled vessels after adding a mixture of nitric- (1.5 mL), hydrochloric (5 mL) - and hydrofluoric acid (0.6 mL) (puriss p.a., Sigma Aldrich – Merck, Darmstadt, Germany). The digests were diluted to 50 mL with deionised water after adding 200 μL internal standard solution (germanium 25 mg L^{-1}).

2.5 Measurement of Mn in PM by mass spectrometry

The element concentrations in the solutions were determined using an Agilent 8800 triple quadrupole inductively coupled plasma mass spectrometer (ICP-MS) (Agilent Technologies, Santa Clara, CA, USA). The instrument was tuned prior to each run, and acid matrix matched standards were prepared for calibration. Details of the ICP-MS setup are given in the ESI (Table S1†).

Reproducibility of the leaching procedure was assessed by use of SiMn and HC–FeMn in-house quality control material. This material is dust collected from the furnace emission electrostatic filters and sieved through 45 μm mesh to remove coarse particles. The total Mn concentrations obtained with the current method were comparable to results obtained by a previously validated method.[38] The precision of the method is defined as the relative standard deviation of $n = 14$ SiMn and $n = 16$ FeMn in-house samples. The precision of Mn was on average 22% for SiMn (~18% $Mn_{dissolved}$) and 13% for HC–FeMn (~27% $Mn_{dissolved}$), respectively. All measured Mn concentrations were above the limit of detection. The limit of detection was calculated as three times the standard deviation of ten blank samples, respectively, 40 ng per filter for acid digested and 7.5 ng per filter for Gamble dissolved.

2.6 Limitations of the leaching method

The bioaccessibility of Mn was studied using Gamble solution. Gamble solution was chosen because it is the most used simulated lung fluid in bioaccessibility studies and facilitates comparison of the results. One alternative to Gamble solution is Hatch solution which additionally contains proteins and enzymes.[29,30,32,39] Hatch solution is, however, more analytically challenging in terms of pH stability, formation of precipitates and filtration compared to Gamble solution.

Extraction time is important in PM dissolution testing.[24] Berlinger *et al.*[29] studied the solubility of Mn and other elements using Gamble and Hatch solutions in different welding fumes

with extraction times between 30 minutes and 24 hours. Further dissolution ceased after 8 hours. Caboche *et al.*[40] suggested that 24 hours is sufficient for dissolution testing of Mn based on ambient air PM of different origins. Based on these two studies, a 24 hour extraction time was chosen in this study.

The solid-to-liquid ratio (S/L ratio) should not be too low in order to avoid unnecessary agglomeration of the PM which may result in a smaller surface area.[39–41] Pelfrêne *et al.*[41] concluded that the S/L ratio influences the PM dissolution when applying Gamble solution. We used a somewhat higher ratio in our study (average: 0.0003, min: 0.00005 max: 0.005 g/10 mL Gamble solution) than what has been found to give the highest bioaccessibility.[39] As the ratio was higher, pronounced agglomeration during the leaching procedure was not expected.

The air samples were collected according to size onto filters. This may lead to increased uncertainty of the estimates of dissolution as the particles are packed onto each other on the filter, and the surface area available for the dissolution is hence reduced. To minimize this effect, shaking of the samples is applied in dissolution testing,[24,39] but would most probably not release all particles from the filters as they are incorporated deep into the filter material or closely packed on the filter surface. However, in our study this effect will most probably not result in significant relative differences in $Mn_{dissolved}$ between SiMn and HC–FeMn production (Smelter 1) or tapper and crane operators (Smelter 2), as we discuss the same size fractions separately. Also, the respirable samples (Table 3) are compared between plant and occupational groups separately from the cascade impactor samples (Fig. 4). The in-house standards of SiMn and HC–FeMn were directly weighed onto the filters and the PM is not packed as the air samples. These samples may therefore have a larger surface area in contact with the Gamble solution. Even in this case, a similar difference in the percentage of $Mn_{dissolved}$ as the collected air samples was observed, 29% for SiMn and 5% for HC–FeMn, respectively.

2.7 Statistical analysis

The percentage of $Mn_{dissolved}$ was calculated from the proportion of the concentration of Gamble dissolved Mn to the total concentration of Mn (concentration of Gamble dissolved plus acid digested). Differences in the dissolved Mn fraction between crane operators and tappers as well as between the furnace area of SiMn and HC–FeMn production were tested with the Wilcoxon rank sum test. We define $p < 0.05$ as statistically significant.

All statistical calculations were performed in R studio version 4.0.4.,[42] and all figures were produced with the package 'ggplot2' version 3.3.2.[43] Wilcoxon rank sum test was calculated with the package 'ggpubr' version 0.4.0.999.[44]

3 Results

3.1 Electron microscopy

The results from electron microscopy are divided in two subchapters. The first subchapter includes characterisation of particles collected directly from the taphole by the electrostatic precipitator. The second subchapter regards particles collected further away from the taphole with the cascade impactor. The two particle sampling procedures were separated to elaborate the differences between particle sizes and particle types collected in the surrounding area of the two work tasks, tapping and crane operation. Particles for characterization were only collected in Smelter 1 where both HC–FeMn and SiMn are produced. The average number size distributions from SMPS measurements in Smelter 1 are shown in Fig. S2† and illustrate that a large number of nanosized (~30 nm) particles exist in the workroom air.

3.1.1 Characterisation of particles collected during tapping with an electrostatic sampler. Samples collected with the electrostatic sampler directly from the taphole of the HC–FeMn and SiMn furnace in Smelter 1 are considered to represent part of the work exposure among tappers. Particle types observed in the tapping fume are summarised in Table 1. Considerable variations in both, chemistry and morphology were found for the condensation particles in the SiMn tapping fume (a summary is given in Table 1). Examples of tapping fume particles collected from the SiMn furnace area are shown in Fig. 1 and 2. Energy-dispersive X-ray microanalysis in SEM and TEM showed that many particles were rich in Si, Mn and O. Larger particles have

Table 1 Summary of particle types collected with an electrostatic sampler from the taphole of SiMn and HC–FeMn furnaces, Smelter 1, during tapping[a]

Process	Particle types
Tapping SiMn furnace	Dominated by condensation particles rich in Mn–Si–O (some particles also have minor amounts of Mg, K and Na) and mixed particles of Mn–O rich crystalline phases surrounded by a Si–O rich amorphous phase. The particles occur as both, individual particles and agglomerates/aggregates. The different particle types were often found in the same agglomerate/aggregate
Tapping HC–FeMn furnace	Dominated by spherical condensation particles of crystalline Mn oxides. These occur as single particles or as aggregates/agglomerates, with primary particle sizes between a few nm and 500 nm. All particles were coated with a few nm thick Si–O-rich surface layer (most likely SiO_2), which holds the primary particles as aggregates

[a] Categories of particle abundance: >50% = dominating; >10% = often; <10% = some.

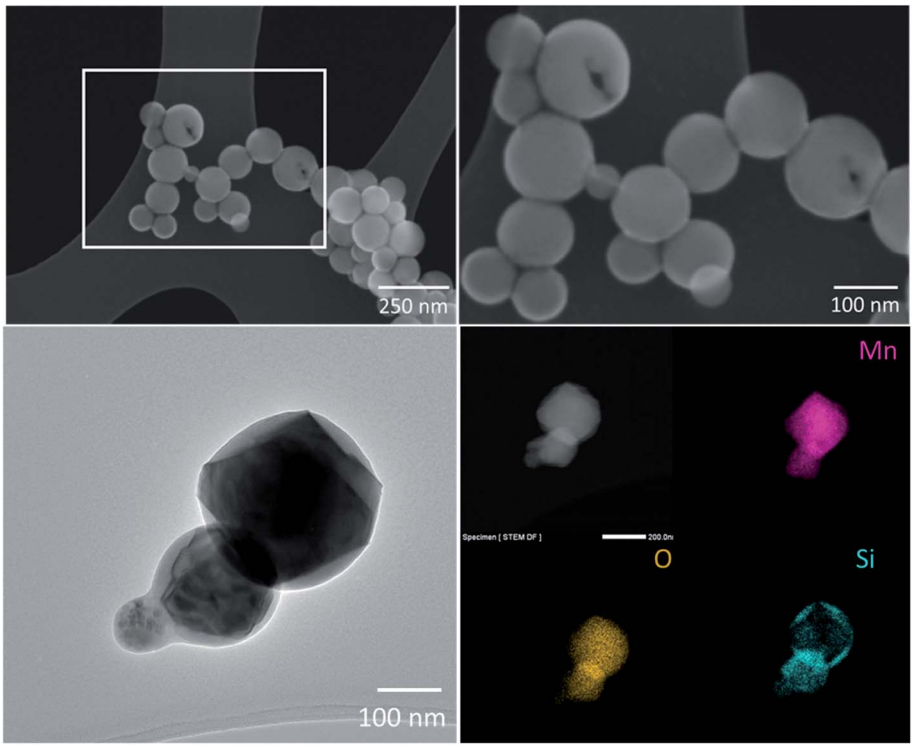

Fig. 1 Secondary electron images of an agglomerate/aggregate (upper left) collected during tapping of the SiMn furnace, and enlargement of the marked area with arrows pointing to holes from the electron bombardment from EDX point analysis (upper right). TEM images of an agglomerate/aggregate (lower left) and the STEM-EDX elemental distribution images for Mn, O, Si (right).

minor amounts of magnesium (Mg), K and sodium (Na). Mixed particles from the SiMn fume consist of angular Mn–O rich crystalline phases which seem to be enclosed in a Si–O rich amorphous matrix (Fig. 1, lower right and Fig. 2). The Mn–O rich phase was identified by SEM-EBSD as hausmannite in some of these mixed particles. The mixed particles and the Si–Mn–O particles often co-existed in agglomerates/aggregates. Single particles were also often observed. Particles collected during tapping of the SiMn furnace were less stable under electron bombardment than particles collected from the HC–FeMn fume, as seen from the two holes in the particles caused by EDX spot analysis (Fig. 1, upper right). It was not possible to determine the phase composition of the Si–Mn–O particles by SEM-EBSD or by TEM-SAED. However, according to TEM, the particles appear to be a mixture of both crystalline and amorphous phases.

The HC–FeMn tapping fume was dominated by spherical primary condensation particles of Mn oxides, which occur as aggregates/agglomerates with sizes up to several μm, or as single particles with a size range from a few nm up to 500 nm. A selection of about 100 primary Mn oxide particles was investigated by SEM-EBSD. Most particles were identified as Mn_3O_4 (hausmannite) and some particles were identified as MnO (manganosite). The hausmannite phase was confirmed by applying TEM-SAED on a few selected particles. Typical particles collected during tapping of the HC–FeMn furnace are shown in Fig. 3. An amorphous Si–O rich surface layer (presumably SiO_2) seems to hold the primary particles together as aggregates (Fig. 3 lower left and lower right). A STEM-EDX elemental line scan for Mn, Si and O of such a particle is shown in Fig. S3.† Please note that the term aggregate will be used for such particles, as the primary particles are held together by chemical forces. When discussing the findings in general or the particles collected from SiMn furnace area (*i.e.*, without a surface layer covering the primary particles), the term agglomerate/aggregate is used. Agglomerates may consist of primary particles and/or aggregates, and it is not always possible to discriminate between agglomerates and aggregates.

3.1.2 Characterisation of particles collected during tapping with the cascade impactor. The stationary cascade impactor was placed around eight meters away from the respective furnaces in Smelter 1. It is assumed that the particles collected here are more representative of the exposure among crane operators than tappers because the crane operators work further away from the furnaces. An overview of the different particle types observed by SEM-EDX in the SiMn and HC–FeMn furnace areas is given in Table 2.

In the furnace area of SiMn production, the first four stages (d_{ae} cut size: 10.0–1.8 μm) were dominated by irregular mixed slag particles, Mn and Fe oxides and coke particles. The slag particles were rich in Si, calcium (Ca), aluminium (Al) and O, with minor amounts of Mg and Mn. The slag particles in the SiMn furnace area had much lower Mn contents than slag particles in the HC–FeMn furnace area. Most particles are inhomogeneous and consist of several phases. An example of a typical particle is shown in the ESI (Fig. S4†).

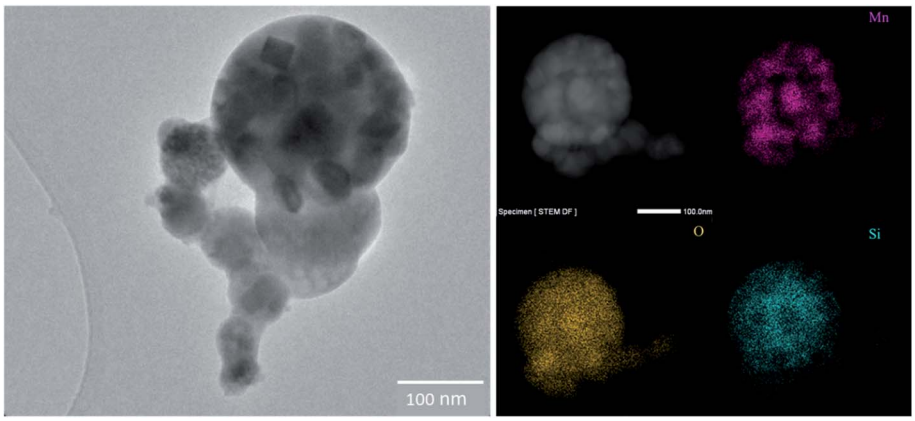

Fig. 2 TEM image of a particle collected from the SiMn tapping fume in Smelter 1 (left) and STEM-EDX elemental distribution images for Mn, O, Si (right).

The next four impactor stages (d_{ae} cut size: 1.0–0.18 μm) are dominated by condensation particles, similar to the particles from the tapping fume (chapter 3.1.1).

The smallest particles (stage 9–13; d_{ae} cut size 0.10–0.010 μm) were dominated by carbonaceous particles. In addition, residues of volatile K and S rich particles were observed. The exact composition of these particles was difficult to determine because these particles were volatile under electron bombardment. Some small agglomerates and single particles of Mn–Si oxides were also observed in stage 9 and 10. Mn containing particles were rare in the last four stages (d_{ae} cut size: 0.056–0.010 μm).

In the furnace area of HC–FeMn production, the first four stages (d_{ae} cut size: 10.0–1.8 μm) were dominated by spherical shaped mixed particles with a high content of K, Na, Cl (often also Zn and Mn) and minor amounts of S and phosphorus (P), as well as irregular shaped particles with a high Mn content. The latter particles often had considerable amounts of Si, Ca and minor amounts of Fe, Al and Mg. The slag in HC–FeMn production is $MnO–SiO_2–CaO$ based. An example of a typical particle encountered can be found in the ESI (Fig. S5 and S6†). Some alloy fragments rich in Mn and Si (minor Fe contents) were observed. Large agglomerates/aggregates of Mn oxides were often found in stage 4 (d_{ae} cut size 5.6 μm).

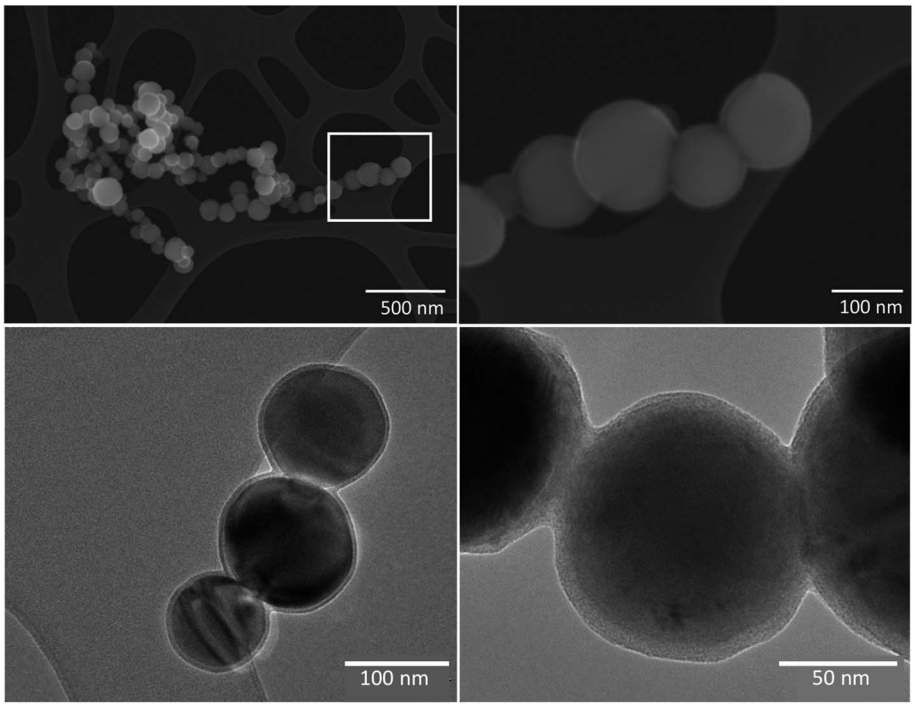

Fig. 3 Secondary electron images of agglomerated/aggregated condensation particles (upper left) collected during tapping of the HC–FeMn furnace. A magnification of the marked area is shown in the upper right image. TEM images of an aggregate: overview (lower left) and magnification showing the primary particles held together by the Si–O layer (lower right).

Table 2 Particle types collected by the cascade impactor in the production facility close to SiMn or FeMn furnaces in Smelter 1[a]

Stages (d_{ae} cut size)	Particle type
SiMn	
1–4 (10.0–1.8 μm)	Dominating: irregular mixed slag particles and Fe and Mn oxides Some: slag particles mixed with coke
5–8 (1.0–0.18 μm)	Dominating: condensation particles rich in Si and Mn oxides (larger condensation particles have minor amounts of Mg), which may co-exist with angular Mn-rich phases identified as hausmannite (Mn_3O_4) and manganosite (MnO) enclosed in a Si–O rich matrix Often: slag particles mixed with oxides of Mn and Fe in stages 5 and 6
9–13 (0.10–0.010 μm)	Dominating: carbonaceous particles (most likely soot) Often: volatile K and/or S rich particles Some: single particles or small aggregates of particles rich in Si and Mn oxides in stage 9 and 10 Rare: single particles or small aggregates of Mn–Si oxides in stages 11, 12 and 13
HC–FeMn	
1–4 (10.0–1.8 μm)	Dominating: spherical particles with high content of K, Na, chlorine (Cl) and O often with high zinc (Zn) and Mn contents, and irregular slag particles with high MnO content Often: large agglomerates/aggregates of Mn oxides in stage 4 Some: large agglomerates/aggregates of Mn oxides stage 1–3 Some: alloy fragments of Mn, Si and Fe
5–8 (1.0–0.18 μm)	Dominating: condensation particles of Mn oxides occurring as aggregates/agglomerates consisting primarily of Mn_3O_4 and MnO. The MnO particles show a Si–O-rich surface layer of a few nm thickness Often: carbonaceous particles (most likely soot)
9–13 (0.10–0.010 μm)	Dominating: carbonaceous particles (most likely soot) Some: single particles or small aggregates of Mn oxides were found in stage 8 and 9 Rare: single particles or small aggregates of Mn oxides in stage 10–13

[a] d_{ae} = aerodynamic diameter. Categories of particle abundance were: dominating > 50%, often > 10%, some < 10%, rare < 2%.

The next three impactor stages (d_{ae} cut size: 1.0–0.32 μm) were dominated by agglomerates/aggregates of spherical Mn oxides. According to TEM-SAED and SEM-EBSD, these particles primarily consist of hausmannite (Mn_3O_4) and manganosite (MnO). The MnO particles were observed with a few nm thick Si–O rich surface layer (Fig. 3).

In stage 8 (d_{ae} cut size: 0.18 μm) and below, carbonaceous particles dominate and only some Mn-rich particles were found. Below stage 9 (d_{ae} cut size: 0.10 μm), Mn-rich particles were rare. In stages 12 and 13 only a few particles were observed (<500).

3.2 Dissolution of Mn in Gamble solution

Total Mn air concentrations in the respirable aerosol fraction and the percentage of $Mn_{dissolved}$ are summarised in Table 3. The air concentrations among tappers were higher compared to crane operators in both Smelter 1 and Smelter 2. The lowest air concentration of total Mn was found among the SiMn production workers.

The median percentage of $Mn_{dissolved}$ among SiMn furnace workers is somewhat higher than that among HC–FeMn furnace workers (Table 3). The $Mn_{dissolved}$ appears to be independent of the work task in Smelter 1. In contrast, the $Mn_{dissolved}$ is significantly higher ($p = 0.008$) for crane operators compared to tappers in HC–FeMn production of Smelter 2.

The percentage of $Mn_{dissolved}$ in air samples collected with the Sioutas cascade impactor was determined as a function of particle size among tappers and crane operators in the SiMn and HC–FeMn production (Fig. 4). In air samples collected from

Table 3 Respirable Mn air concentration [μg m^{-3}] and percentage of $Mn_{dissolved}$ (in parenthesis) in the breathing zone of crane operators and tappers working in SiMn and HC–FeMn smelters

	SiMn		HC–FeMn			
Location	Smelter 1		Smelter 1		Smelter 2	
Work task	Crane operators $n = 5$	Tappers $n = 5$	Crane operators $n = 5$	Tappers $n = 4$	Crane operators $n = 8$	Tappers $n = 10$
Minimum	7.2 (15)	6.8 (12)	17.0 (6)	21.4 (8)	12.2 (4)	26.0 (2)
Lower quartile	11.3 (20)	21.5 (17)	31.7 (7)	46.3 (10)	15.6 (7)	35.0 (3)
Median	14.6 (23)	23.5 (20)	39.5 (11)	55.0 (12)	24.5 (10)	40.6 (4)
Upper quartile	14.8 (25)	26.9 (21)	43.2 (12)	56.3 (17)	29.7 (14)	53.8 (6)
Maximum	17.0 (27)	65.0 (44)	43.5 (18)	59.5 (30)	46.9 (18)	115.0 (7)

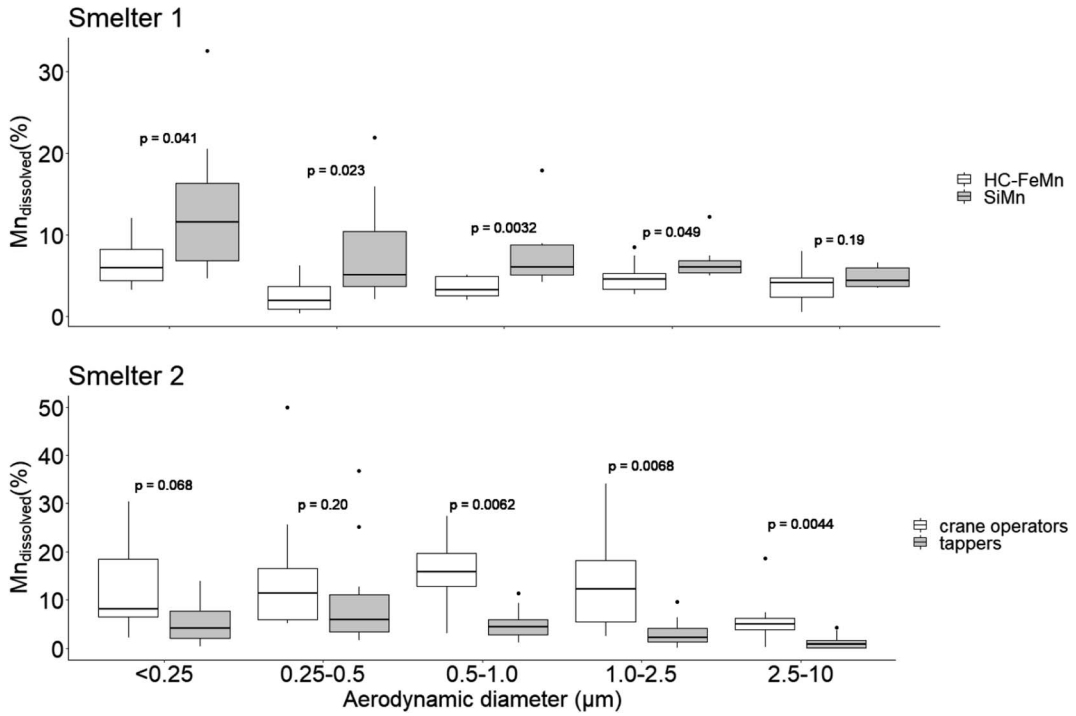

Fig. 4 Percentage of $Mn_{dissolved}$ as a function of particle size (aerodynamic diameter) for HC–FeMn and SiMn workers in Smelter 1 and crane operators and tappers in Smelter 2. In each size fraction, the number of samples was 10 for SiMn and 9 for HC–FeMn (Smelter 1), as well as 8 crane operator (7 in size fraction 1.0–2.5) and 10 tappers (Smelter 2). *P*-values between the respective groups are presented for each size bin.

HC–FeMn workers in Smelter 1, the percentage of $Mn_{dissolved}$ is independent of d_{ae} particle size except for a small increase for particles < 0.25 μm. In contrast, in air samples from SiMn furnace workers, $Mn_{dissolved}$ increases with decreasing particle size (Fig. 4, Smelter 1). The percentage of $Mn_{dissolved}$ is significantly higher for SiMn than in HC–FeMn workers for particle d_{ae} sizes up to 2.5 μm. The Mn air concentration in PM collected with the Sioutas cascade impactor is given in the ESI (Fig. S1†).

In the air samples from the HC–FeMn workers in Smelter 2 (Fig. 4, Smelter 2), the percentage of $Mn_{dissolved}$ is similar in all size fractions for both crane operators and tappers. However, the percentage of $Mn_{dissolved}$ is considerably higher (by a factor of 2–5) with a larger variation within the size fractionated samples among crane operators compared to tappers. In general, the percentage of $Mn_{dissolved}$ is low for workers in Smelter 2, and lowest for tappers (Table 3). Tappers have slightly higher air concentrations of Mn in d_{ae} size fractions below 2.5 μm compared to crane operators (Fig. S1†).

4 Discussion

There were substantial differences in the morphology, chemical composition and microstructure between particles collected in the furnace area of SiMn production compared to particles collected in the furnace area of HC–FeMn production in Smelter 1. Typically, the dominating Mn oxide particles in the HC–FeMn furnace area were crystalline and had a thin amorphous Si–O surface layer which seemed to hold the particles as aggregates. Both crystalline and amorphous Mn and Si containing oxides were observed in the SiMn tapping fume, but a Si–O surface layer was not observed. The Mn oxide particles observed in the SiMn tapping fume were enclosed in an amorphous Si–O matrix. Nanometre sized particles containing Mn were rarely found in the size bins below 100 nm in any of the smelters. Carbonaceous particles, most probably soot from combustion, dominated the smallest size fraction (<180 nm).

In general, the percentage of $Mn_{dissolved}$ was low to moderate (<30%) in both type of smelters. A significantly higher percentage of $Mn_{dissolved}$ was observed in the SiMn furnace area compared to the HC–FeMn furnace area. In the size fractionated samples, this difference was significant for particles between <0.25 and 2.5 μm.

4.1 Particle characterisation

Collection of particles for characterization was only performed in Smelter 1. The particles collected in the tapping process of HC–FeMn in Smelter 1 are considered to be representative of the fume particles formed in Smelter 2 as the raw materials and the production process are identical. However, the fact that some contamination from the SiMn production process will occur cannot be excluded. Slag particles and spherical particles rich in K, Na, Cl, Zn and O dominated the fraction above d_{ae} of 1 μm in fume collected from the HC–FeMn furnace (Table 2). Sources may be raw materials, which always contain Zn, K and Na that partly evaporate in the smelting process. Particles below 2 μm rich in K with various amounts of Na, S, Zn, Cl and O were reported by Gjønnes *et al.*,[18] and high mass concentrations of K in PM were found by Gunst *et al.*[17] In the present study, K rich particles with

d_{ae} < 1 μm surround the larger spherical K, Na, Cl rich particles (Fig. S5†). Additionally, Mn rich areas were often found inside of these larger particles (Fig. S5†). Larger particles of slag and carbonaceous particles seem to be sintered together in the SiMn furnace area which corresponds to the observations by Gunst *et al.*[17] In agreement with previous observations,[17,18] particles with d_{ae} > 1 μm were generally inhomogeneous and irregular in shape.

Particles collected during tapping of HC–FeMn in the d_{ae} size range 0.18–1 μm were dominated by crystalline Mn oxide particles (MnO and Mn_3O_4). This is in accordance with the results of Gjønnes *et al.*,[18] except that they additionally observed MnO fibers during tapping of HC–FeMn. Furthermore, Ervik *et al.*[19] analysed particles by SEM-EBSD and identified hausmannite (Mn_3O_4) as the dominating Mn oxide. Agglomerated spheres of Mn oxides dominated the d_{ae} size range from 0.09 to 0.94 μm in particles studied by Kero, Slizovskiy,[45] which is in good agreement with the results of our study (Table 2). Our SEM and TEM observations indicate that the primary particles collected in HC–FeMn tapping fume are held together by an amorphous Si–O rich surface layer. The presence of such surface layers may have implications for the behaviour and toxicity of the particles, *e.g.* such as a higher resistance of breakdown or collapse of the aggregate/agglomerate in the lung.[46] Additionally, micrometre sized particles are reported to be phagocytized more easily than nanometre sized particles.[47,48]

In our study, a complex mix of condensation particles was found in the SiMn fume (*e.g.* mixture of Mn_3O_4 and Si–O, as well as amorphous and crystalline Si–Mn–O rich particles). Ma *et al.*[21] observed similar particles in SiMn fume from an experimental setup and identified Mn_2SiO_4 as well as Mn_3O_4 in the fume at melting temperatures of 1500–1700 °C. In accordance with their findings, we also observed angular Mn_3O_4 phases, often mixed with an amorphous Si–O phase. The molten metal will react with oxygen in the air and the observation of various MnSi phases in Gjønnes *et al.*[18] (in, *e.g.*, Mn_3Si, Mn_6Si and Mn_5Si_2) from SiMn casting is therefore surprising. Some particles collected during tapping of the SiMn furnace consisted of nanometre sized Mn rich phases enclosed in a Si–O rich matrix (Fig. 1 and 2). A silica precursor has been used in previous investigations as an additive in shielding gas in welding. The resulting amorphous silica formed a coating that encapsulated the welding fume particles[49] leading to formation of larger particles that may change the deposition efficiency in the lungs. However, amorphous silica particles have earlier shown to have a low retention in rat lungs explained by a high solubility.[50] Considering this in our work, a high solubility of the Si–O rich layer may expose the Mn rich phases.

Carbonaceous particles dominate the d_{ae} size fraction below 0.18 μm, both in HC–FeMn and SiMn furnace area, with some single particles and small agglomerates of Mn oxides and Mn–Si oxides. The fact that few nanometre sized Mn containing particles were observed, and instead seem to be bound in aggregates/agglomerates, is an important finding. This is because a change in particle size affects the deposition fate upon inhalation. In addition, translocation of particles to other organs is only relevant for the smallest particles. It should also be noted that even though few particles were observed in the last two stages of the cascade impactor, it is likely that particles of this size exist in large numbers as is shown in the particle size distribution (Fig. S2†) and observed in this industry previously.[20,33] Residues of secondary organic particles have been found from combustion in high temperature industrial processes, as was found, for example, in an Al plant.[51] Such small secondary particles evaporate under electron bombardment in EM. Secondary organic particles might also exist in the workroom air of Mn smelters. In addition, small soot particles below d_{ae} of 30 nm are not easily detected in SEM.

4.2 Bioaccessibility

Our study shows that the percentage of $Mn_{dissolved}$ is low to moderate (<30%), which is comparable to what was reported close to an FeMn production plant and steel making industry.[28] However, the percentage of $Mn_{dissolved}$ is higher in our samples than in PM collected from different welding fumes dissolved in Gamble solution[29] indicating a lower bioaccessibility of the latter. A higher Mn dissolution in Hatch than Gambles has been reported for Mn in welding fumes.[29]

The percentage of $Mn_{dissolved}$ was higher in PM collected among SiMn furnace workers compared to HC–FeMn furnace workers. The largest difference in the percentage of $Mn_{dissolved}$ was observed for PM with d_{ae} between 0.25 and 1.0 μm. This size range is dominated by agglomerates and agglomerates/aggregates of primary particles. Gjønnes *et al.*[18] suggested a higher health risk for workers exposed to Mn in HC–FeMn compared to SiMn production. Their conclusion was based on the assumption that Mn oxides are more soluble than SiMn, as was shown by Thomassen *et al.*[52] We observed a surface layer of amorphous Si–O on MnO-containing particles in the HC–FeMn furnace area holding the primary particles together into agglomerates/aggregates. Such an amorphous layer was not observed for particles in the SiMn fume. Instead, Mn rich crystalline phases were encapsulated in a Si rich amorphous matrix (Fig. 3). Amorphous and crystalline Si–Mn–O rich particles without a surface layer or an additional matrix were also observed. Amorphous SiO_2 has been shown to dissolve substantially in Gamble solution.[53] The higher percentage of $Mn_{dissolved}$ in SiMn fume PM may, thus, be a result of the amorphous Si–O matrix dissolving in Gamble solution and releasing small Mn rich phases.

The air concentration of Mn [μg m^{-3}] in PM was higher in the breathing zone of tappers compared to that of the crane operators (Table 3). This result was not unexpected, as it has been previously shown that the tappers were exposed to a statistically significant higher mass concentration of PM than the crane operators.[33] The difference in $Mn_{dissolved}$ is, however, only statistically significant between crane operators and tappers in Smelter 2, which only included a HC–FeMn furnace. The largest differences in $Mn_{dissolved}$ between tappers and crane operators are observed for PM with d_{ae} > 500 nm, representing most of the mass.[33] In this size fraction, we found irregular slag particles with high MnO content and particles with higher amount of Mn and Zn, as well as minor amounts of K, Na and Cl. The particle composition in different working areas of the HC–FeMn smelter

was also studied by Gunst *et al.*,[17] and a different chemical composition of PM collected among tappers and crane operators was found. Particulate matter collected among tappers contained higher mass fractions of K, Na and Zn than among crane operators. In our study, a dominating fraction of the particles observed in the first stages of the cascade impactor contained K, Na, Cl and Zn together with Mn, but such particles did not dominate in samples collected directly from the tapping fume with the electrostatic sampler. The amount of such particles may explain the difference in the percentage of $Mn_{dissolved}$ between tappers and crane operators. The difference from Gunst's[17] study may be a result of the composition of the raw material used in the production during sampling. Further investigations are needed to conclude on the observed difference in bioaccessible Mn between tappers and crane operators in the HC–FeMn industry.

4.3 Conclusion

Detailed SEM and TEM analysis of samples collected in the furnace hall of HC–FeMn and SiMn production showed different particle types related to work area and task. The results of this study indicate that the different physicochemical characteristics of the particles might explain the difference in $Mn_{dissolved}$ seen in PM samples collected by the workers in this industry. Still, further investigations are needed to conclude if the difference in $Mn_{dissolved}$ is related to the dissolution of the Si-matrix observed in particles collected from the SiMn tapping fume.

Our results show that the concentration of Mn in PM in air was significantly higher for tappers and crane operators, but the $Mn_{dissolved}$ was significantly lower for tappers than crane operators. Further research is needed to investigate if this difference in $Mn_{dissolved}$ between crane operators and tappers is related to the physicochemical properties of the particles.

In conclusion, the results have shown that connecting the knowledge of particle characteristics and bioaccessibility is important to gain more information on how particles may behave in contact with lung fluids. The physicochemical properties of single particles and Mn bioaccessibility are key factors to be considered in risk assessment. With regards to this, our size resolved data on particle characteristics and bioaccessibility give additional information which can be combined with what is already known about the particle size dependent deposition efficiency in lungs. Furthermore, the results of this study can be applied in future epidemiological studies and toxicological assays.

Funding

This study was partly funded by the Sickness Absence, Work and Health programme of the Norwegian Research Council under grant 218350 and partly by the Confederation of Norwegian Enterprise Working Environment Fund.

Author contributions

SEH conducted the dissolution tests, analysed the samples by ICP-MS, performed data analysis and wrote the manuscript. TE performed sampling and SEM analysis, and participated in the discussion of the results and manuscript writing. NB carried out the TEM analyses. SW helped with statistical analysis, participated in discussion of the results and manuscript writing. YT and DGE took part in the study initiation, participated in the discussion of results as well as preparation and reviewing of the manuscript. BBE performed sampling and was engaged in the study design, discussion of the results as well as manuscript preparation and reviewing.

Conflicts of interest

There are no conflicts to declare.

Acknowledgements

The authors gratefully acknowledge the financially support from the funders. SEH would like to thank Stephen Dorn and Jon Hovik for their skilled laboratory work.

References

1 H. Roels, G. Meiers, M. Delos, I. Ortega, R. Lauwerys, J. P. Buchet, *et al.*, Influence of the route of administration and the chemical form (MnCl2, MnO2) on the absorption and cerebral distribution of manganese in rats, *Arch. Toxicol.*, 1997, **71**(4), 223–230.

2 D. C. Dorman, M. F. Struve, R. A. James, M. W. Marshall, C. U. Parkinson and B. A. Wong, Influence of Particle Solubility on the Delivery of Inhaled Manganese to the Rat Brain: Manganese Sulfate and Manganese Tetroxide Pharmacokinetics Following Repeated (14-Day) Exposure, *Toxicol. Appl. Pharmacol.*, 2001, **170**(2), 79–87.

3 D. G. Ellingsen, R. Konstantinov, R. Bast-Pettersen, L. Merkurjeva, M. Chashchin, Y. Thomassen, *et al.*, A neurobehavioral study of current and former welders exposed to manganese, *Neurotoxicology*, 2008, **29**(1), 48–59.

4 F. Taube, Manganese in occupational arc welding fumes—aspects on physiochemical properties, with focus on solubility, *Ann. Occup. Hyg.*, 2013, **57**(1), 6–25.

5 Z. Long, Y.-M. Jiang, X.-R. Li, W. Fadel, J. Xu, C.-L. Yeh, *et al.*, Vulnerability of welders to manganese exposure–A neuroimaging study, *Neurotoxicology*, 2014, **45**, 285–292.

6 S. R. Criswell, S. S. Nielsen, M. N. Warden, H. P. Flores, J. Lenox-Krug, S. Racette, *et al.*, MRI Signal Intensity and Parkinsonism in Manganese-Exposed Workers, *Occup. Environ. Med.*, 2019, **61**(8), 641–645.

7 J. Rodier, Manganese poisoning in Moroccan miners, *Br. J. Ind. Med.*, 1955, **12**(1), 21.

8 W. W. Dlamini, G. Nelson, S. S. Nielsen and B. A. Racette, Manganese exposure, parkinsonian signs, and quality of life in South African mine workers, *Am. J. Ind. Med.*, 2020, **63**(1), 36–43.

9 A. M. Emara, S. H. El-Ghawabi, O. I. Madkour and G. H. El-Samra, Chronic manganese poisoning in the dry battery industry, *Br. J. Ind. Med.*, 1971, **28**(1), 78.

10 H. A. Roels, P. Ghyselen, J. P. Buchet, E. Ceulemans and R. R. Lauwerys, Assessment of the permissible exposure level to manganese in workers exposed to manganese dioxide dust, *Br. J. Ind. Med.*, 1992, **49**(1), 25–34.
11 J.-D. Wang, C. Huang, Y. Hwang, J. Chiang, J. Lin and J. Chen, Manganese induced parkinsonism: an outbreak due to an unrepaired ventilation control system in a ferromanganese smelter, *Occup. Environ. Med.*, 1989, **46**(12), 856–859.
12 R. Bast-Pettersen, D. G. Ellingsen, S. M. Hetland and Y. Thomassen, Neuropsychological function in manganese alloy plant workers, *Int. Arch. Occup. Environ. Health*, 2004, **77**(4), 277–287.
13 M. Bouchard, D. Mergler, M. E. Baldwin and M. Panisset, Manganese cumulative exposure and symptoms: a follow-up study of alloy workers, *Neurotoxicology*, 2008, **29**(4), 577–583.
14 L. Holappa. *Handbook of Ferroalloys: Chapter 2. Basics of Ferroalloys*, Elsevier Science, 2013.
15 S. E. Olsen, S. Olsen, M. Tangstad and T. Lindstad, *Production of Manganese Ferroalloys*: Tapir academic press, 2007.
16 I. T. Kero, P. A. Eidem, Y. Ma, H. Indresand, T. A. Aarhaug and S. Grådahl, Airborne Emissions from Mn Ferroalloy Production, *JOM*, 2019, **71**(1), 349–365.
17 S. Gunst, S. Weinbruch, M. Wentzel, H. M. Ortner, A. Skogstad, S. Hetland, *et al.*, Chemical composition of individual aerosol particles in workplace air during production of manganese alloys, *J. Environ. Monit.*, 2000, **2**(1), 65–71.
18 K. Gjønnes, A. Skogstad, S. Hetland, D. G. Ellingsen, Y. Thomassen and S. Weinbruch, Characterisation of workplace aerosols in the manganese alloy production industry by electron microscopy, *Anal. Bioanal. Chem.*, 2011, **399**(3), 1011–1020.
19 T. K. Ervik, N. Benker, S. Weinbruch, A. Skogstad, Y. Thomassen, D. G. Ellingsen, *et al.*, Phase identification of individual crystalline particles by combining EDX and EBSD: application to workplace aerosols, *Anal. Bioanal. Chem.*, 2018, **410**(11), 2711–2721.
20 I. Kero, M. K. Naess and G. Tranell, Particle size distributions of particulate emissions from the ferroalloy industry evaluated by electrical low pressure impactor (ELPI), *J. Occup. Environ. Hyg.*, 2015, **12**(1), 37–44.
21 Y. Ma, I. Kero and G. Tranell, Fume formation from oxidation of liquid SiMn alloy, *Oxid. Met.*, 2018, **89**(1–2), 211–231.
22 J. C. Ng, A. Juhasz, E. Smith and R. Naidu, Assessing the bioavailability and bioaccessibility of metals and metalloids, *Environ. Sci. Pollut. Res.*, 2015, **22**(12), 8802–8825.
23 F. Kastury, E. Smith and A. L. Juhasz, A critical review of approaches and limitations of inhalation bioavailability and bioaccessibility of metal (loid) s from ambient particulate matter or dust, *Sci. Total Environ.*, 2017, **574**, 1054–1074.
24 C. L. Wiseman, Analytical methods for assessing metal bioaccessibility in airborne particulate matter: a scoping review, *Anal. Chim. Acta*, 2015, **877**, 9–18.
25 O. Moss, Simulants of lung interstitial fluid, *Health Phys.*, 1979, **36**(3), 447–448.
26 H. Ren, Y. Yu and T. An, Bioaccessibilities of metal(loid)s and organic contaminants in particulates measured in simulated human lung fluids: A critical review, *Environ. Pollut.*, 2020, **265**, 115070.
27 M. Kendall, Fine airborne urban particles (PM2.5) sequester lung surfactant and amino acids from human lung lavage, *Am. J. Physiol.: Lung Cell. Mol. Physiol.*, 2007, **293**(4), L1053–L1058.
28 S. Mbengue, L. Y. Alleman and P. Flament, Bioaccessibility of trace elements in fine and ultrafine atmospheric particles in an industrial environment, *Environ. Geochem. Health*, 2015, **37**(5), 875–889.
29 B. Berlinger, D. G. Ellingsen, M. Náray, G. Záray and Y. Thomassen, A study of the bio-accessibility of welding fumes, *J. Environ. Monit.*, 2008, **10**(12), 1448–1453.
30 D. G. Ellingsen, E. Zibarev, Z. Kusraeva, B. Berlinger, M. Chashchin, R. Bast-Pettersen, *et al.*, The bioavailability of manganese in welders in relation to its solubility in welding fumes, *Environ. Sci: Process. Impacts*, 2013, **15**(2), 357–365.
31 B. Berlinger, S. Weinbruch, D. G. Ellingsen, E. Zibarev, V. Chashchin, M. Chashchin, *et al.*, On the bio-accessibility of 14 elements in welding fumes, *Environ. Sci.: Processes Impacts*, 2019, **21**(3), 497–505.
32 B. Berlinger, U. Skogen, C. Meijer and Y. Thomassen, Workplace exposure to particulate matter, bio-accessible, and non-soluble metal compounds during hot work processes, *J. Occup. Environ. Hyg.*, 2019, **16**(6), 378–386.
33 B. Berlinger, M. D. Bugge, B. Ulvestad, H. Kjuus, K. Kandler and D. G. Ellingsen, Particle size distribution of workplace aerosols in manganese alloy smelters applying a personal sampling strategy, *Environ. Sci: Process. Impacts*, 2015, **17**(12), 2066–2073.
34 A. Miller, G. Frey, G. King and C. A. Sunderman, Handheld Electrostatic Precipitator for Sampling Airborne Particles and Nanoparticles, *Aerosol Sci. Technol.*, 2010, **44**, 417–427.
35 Y. Fujitani, S. Hasegawa, A. Fushimi, Y. Kondo, K. Tanabe, S. Kobayashi, *et al.*, Collection characteristics of low-pressure impactors with various impaction substrate materials, *Atmos. Environ.*, 2006, **40**(18), 3221–3229.
36 T. K. Ervik, N. Benker, S. Weinbruch, Y. Thomassen, D. G. Ellingsen and B. Berlinger, Size distribution and single particle characterization of airborne particulate matter collected in a silicon carbide plant, *Environ. Sci: Process. Impacts*, 2019, **21**(3), 564–574.
37 J. Schindelin, I. Arganda-Carreras, E. Frise, V. Kaynig, M. Longair, T. Pietzsch, *et al.*, Fiji: an open-source platform for biological-image analysis, *Nat. methods*, 2012, **9**(7), 676–682.
38 Y. Thomassen, E. Nieboer, D. Ellingsen, S. Hetland, T. Norseth, J. Øyvind Odland, *et al.*, Characterisation of

workers' exposure in a Russian nickel refinery, *J. Environ. Monit.*, 1999, **1**(1), 15–22.

39 F. Kastury, E. Smith, R. R. Karna, K. G. Scheckel and A. Juhasz, An inhalation-ingestion bioaccessibility assay (IIBA) for the assessment of exposure to metal (loid) s in PM10, *Sci. Total Environ.*, 2018, **631**, 92–104.

40 J. Caboche, E. Perdrix, B. Malet and L. Y. Alleman, Development of an in vitro method to estimate lung bioaccessibility of metals from atmospheric particles, *J. Environ. Monit.*, 2011, **13**(3), 621–630.

41 A. Pelfrêne, M. R. Cave, J. Wragg and F. Douay, In vitro investigations of human bioaccessibility from reference materials using simulated lung fluids, *Int. J. Environ. Res. Public Health*, 2017, **14**(2), 112.

42 RStudio, *RStudio: Integrated Development for R*. RStudio, Inc, Boston, MA, 2015, http://www.rstudio.com.

43 H. Wickham, *ggplot2: Elegant Graphics for Data Analysis. Version 3.3.2*, Springer-Verlag, New York; 2016, available at: https://ggplot2.tidyverse.org.

44 A. A. Kassambara*ggpubr: 'ggplot2' Based Publication Ready Plots. Version: 0.4.0*, 2020, available at: https://rpkgs.datanovia.com/ggpubr/.

45 I. Kero, D. Slizovskiy, B. Wittgens and G. Tranell Fume Formation from Liquid Ferromanganese. Sustainable Industrial Processing Summit, *Takano Intl. Symp. On Metals and Alloys*, vol. 3. 2015.

46 J. Pauluhn. Common Denominators of Carbon Nanotubes, in *Nanomaterials*, ed. (DFG) DF, Wiley-VCH Verlag GmbH & Co., Bonn, Germany, 2013, pp. 68–83.

47 H. M. Braakhuis, M. V. D. Z. Park, I. Gosens, W. H. De Jong and F. R. Cassee, Physicochemical characteristics of nanomaterials that affect pulmonary inflammation, *Part. Fibre Toxicol.*, 2014, **11**(1), 18.

48 M. Riediker, D. Zink, W. Kreyling, G. Oberdörster, A. Elder, U. Graham, *et al.*, Particle toxicology and health - where are we? Part, *Fibre Toxicol*, 2019, **16**(1), 19.

49 N. Topham, J. Wang, M. Kalivoda, J. Huang, K.-M. Yu, Y.-M. Hsu, *et al.*, Control of Cr6+ emissions from gas metal arc welding using a silica precursor as a shielding gas additive, *Ann. Occup. Hyg.*, 2012, **56**(2), 233–241.

50 M. P. Sutunkova, S. N. Solovyeva, B. A. Katsnelson, V. B. Gurvich, L. I. Privalova, I. A. Minigalieva, *et al.*, A paradoxical response of the rat organism to long-term inhalation of silica-containing submicron (predominantly nanoscale) particles of a collected industrial aerosol at realistic exposure levels, *Toxicology*, 2017, **384**, 59–68.

51 Y. Thomassen, W. Koch, W. Dunkhorst, D. G. Ellingsen, N. P. Skaugset, L. Jordbekken, *et al.*, Ultrafine particles at workplaces of a primary aluminium smelter, *J. Environ. Monit.*, 2006, **8**(1), 127–133.

52 Y. Thomassen, D. G. Ellingsen, S. Hetland and G. Sand, Chemical speciation and sequential extraction of Mn in workroom aerosols: analytical methodology and results from a field study in Mn alloy plants, *J. Environ. Monit.*, 2001, **3**(6), 555–559.

53 R. R. Larson, S. G. Story and K. T. Hegmann, Assessing the solubility of silicon dioxide particles using simulated lung fluid, *The Open Toxicol. J.*, 2010, **4**(1), 51–55.